

How linear is wall-bounded turbulence?

Javier Jiménez

Citation: *Phys. Fluids* **25**, 110814 (2013); doi: 10.1063/1.4819081

View online: <http://dx.doi.org/10.1063/1.4819081>

View Table of Contents: <http://pof.aip.org/resource/1/PHFLE6/v25/i11>

Published by the [AIP Publishing LLC](#).

Additional information on Phys. Fluids

Journal Homepage: <http://pof.aip.org/>

Journal Information: http://pof.aip.org/about/about_the_journal

Top downloads: http://pof.aip.org/features/most_downloaded

Information for Authors: <http://pof.aip.org/authors>

ADVERTISEMENT



Running in Circles Looking for the Best Science Job?

Search hundreds of exciting
new jobs each month!

<http://careers.physicstoday.org/jobs>

physicstodayJOBS



How linear is wall-bounded turbulence?

Javier Jiménez

School of Aeronautics, Universidad Politécnica de Madrid, 28040 Madrid, Spain

(Received 17 February 2013; accepted 10 May 2013; published online 11 September 2013)

The relevance of Orr's inviscid mechanism to the transient amplification of disturbances in shear flows is explored in the context of bursting in the logarithmic layer of wall-bounded turbulence. The linearized problem for the wall normal velocity is first solved in the limit of small viscosity for a uniform shear and for a channel with turbulent-like profile, and compared with the quasiperiodic bursting of fully turbulent simulations in boxes designed to be minimal for the logarithmic layer. Many properties, such as time and length scales, energy fluxes between components, and inclination angles, agree well between the two systems. However, once advection by the mean flow is subtracted, the directly computed linear component of the turbulent acceleration is found to be a small part of the total. The temporal correlations of the different quantities in turbulent bursts imply that the classical model, in which the wall-normal velocities are generated by the breakdown of the streamwise-velocity streaks, is a better explanation than the purely autonomous growth of linearized bursts. It is argued that the best way to reconcile both lines of evidence is that the disturbances produced by the streak breakdown are amplified by an Orr-like transient process drawing energy directly from the mean shear, rather than from the velocity gradients of the nonlinear streak. This, for example, obviates the problem of why the cross-stream velocities do not decay once the streak has broken down. © 2013 Author(s). All article content, except where otherwise noted, is licensed under a Creative Commons Attribution 3.0 Unported License. [<http://dx.doi.org/10.1063/1.4819081>]

I. INTRODUCTION

There is widespread agreement that turbulence requires the nonlinearity of the Navier–Stokes equations. Neither the multiscale inertial energy cascade¹ nor the characteristic sensitivity to initial conditions,² can exist in a statistically steady linear system. Nevertheless, there is also clear evidence that at least some aspects of shear turbulence are controlled by linear processes, especially in the energy-injection range. The best-known examples are the inflection-point linearized instabilities of the mean velocity profile,³ which are known to represent well many of the properties of the large-scale structures in fully nonlinear free-shear flows, especially forced ones.⁴ The mean profiles of wall-bounded turbulent flows are known to be linearly stable,^{5,6} but there have been repeated attempts to relate their largest scales to linearized instabilities,^{7–10} even predating the understanding of that relation in the free-shear case. The general idea is that the ultimate energy source for turbulent fluctuations in a shear flow is the velocity difference across the mean profile, and that the main energy-production mechanism, the deformation of the profile by cross-shear velocities, is contained in the linearized equations. A key breakthrough took place when it was realized in the early 1990s that even linearly stable perturbations could grow substantially by extracting energy from the mean flow. For a review of such “transient-growth” mechanisms, see Ref. 11.

In practice, the argument only applies to the largest scales. The condition for linearization is roughly that the time scale of the fluctuations, $O(\lambda/u_\lambda)$, where λ and u_λ are characteristic length and velocity scales, should be slow with respect to the mean shear S . If we assume the inertial relation,¹ $u_\lambda \approx (\varepsilon\lambda)^{1/3}$, where ε is the energy dissipation rate, the linearizability condition becomes $\lambda > L_c = (\varepsilon/S^3)^{1/2}$. The scale L_c was introduced by Corrsin¹² as a limit for small-scale anisotropy, and later confirmed experimentally for boundary layers.¹³ If we take q' to be a typical velocity fluctuation

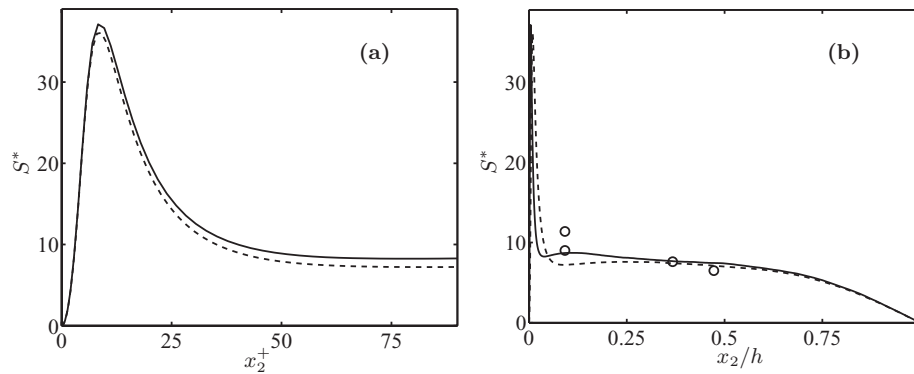


FIG. 1. Shear parameter in wall-bounded turbulent flows, as a function of the distance to the wall. —, channel C2000 in Table I; ---, channel C950; \circ , high-Reynolds-number boundary layer.¹³ (a) Wall scaling. (b) Outer scaling.

intensity in an equilibrium shear flow in which ε can be assumed to be of the order of the turbulent energy production, $\varepsilon \approx q'^2 S$, the Corrsin scale is of the order of the integral energy scale $L_\varepsilon = q'^3/\varepsilon$. The ratio between the Corrsin and integral lengths is often given in terms of the shear parameter $S^* = Sq'^2/\varepsilon = (L_\varepsilon/L_c)^{2/3}$, which should be large for linearization. That is satisfied in the buffer layer of wall-bounded turbulence, where $S^* \approx 40$ (see Figure 1(a)), and the flow in that region is known to share many features with linearized rapid-distortion theory.¹⁴ We will be interested here in the logarithmic layer farther from the wall ($x_2^+ \gtrsim 50$ in this context), where the shear parameter is $S^* \approx 10$ (see Figure 1(b)). In the central part of channels ($x_2/h \gtrsim 0.6$), where the shear is even weaker, linearization is unlikely to be relevant.

We denote by x_1 to x_3 the streamwise, cross-shear, and spanwise directions and by h the thickness of the flow, usually the half-width of a channel. The “+” superscript refers to quantities normalized with the kinematic viscosity ν and with the friction velocity u_τ .

The key property of the inflection-point instabilities that control free-shear flows is that they are essentially inviscid, and that, being already present in the inviscid linearized equations, their evolution time is $O(1/S)$. Viscous instabilities such as the Tollmien-Schlichting waves found in the transition of wall-bounded flows have much slower characteristic times,¹⁵ and cannot compete with the nonlinear deformation of even the largest turbulent eddies.

If we restrict ourselves to parallel or weakly non-parallel shear flows, there are two main inviscid linearized growth mechanisms that apply to stable mean velocity profiles. The first one was proposed by Orr,¹⁶ and does not directly inject net energy into the flow. The cross-shear velocity is amplified when backwards-leaning perturbations are tilted forward by the shear until they are roughly normal to it, and is damped again as they continue to be tilted past that point. The amplification mechanism is driven by continuity, and therefore by pressure, which inhibits the cross-shear velocity when the structures are strongly tilted, and releases that inhibition when they are closer to vertical (see Figure 2(a)).

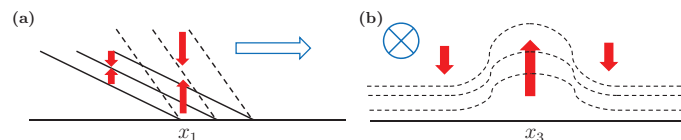


FIG. 2. (a) Sketch of the Orr mechanism. The shear is parallel to the plane of the figure, and tilts velocity structures to the right. As it does (solid to dashed lines), the horizontal spacing of the structures does not change, but the vertical one increases, and continuity requires higher wall-normal velocities. (b) Sketch of the lift-up. The shear is into the page, represented by the upwards-increasing dashed isolines of the streamwise velocity. The wall-normal velocity perturbations deform the mean profile to create long streaks of the streamwise velocity. Although both processes are pictured here as two-dimensional, in the (x_1-x_2) streamwise plane in (a), and in the (x_2-x_3) cross-plane in (b), both also act on oblique waves, leading to three-dimensional perturbations.

In the second mechanism, usually known as lift-up, the cross-shear velocities deform the mean profile to create perturbations of the streamwise velocity component, which do not disappear as the cross-stream perturbations decay (see Figure 2(b)). Because it results in a net creation of turbulent energy, the lift-up was soon implicated in the maintenance of wall-bounded turbulence,¹⁷ and specifically in the formation of the streamwise-velocity streaks.¹⁸

Potentially, the Orr and lift-up mechanisms form a hierarchical pair in which the former generates a transient cross-shear velocity, which in turn creates a streamwise streak that only decays slowly by viscosity.

That combination results in a net creation of fluctuation energy, but for linearly stable profiles such as those in wall-bounded flows, the net result can only be transient. The generation of the cross-shear velocity in wall-bounded turbulence has more often been associated with the instability of finite-amplitude streaks.¹⁹ That conceptual model, developed mostly for the buffer region, is a nonlinear cycle in which the cross-shear velocity, in the form of quasi-streamwise vortices, generates streaks that grow until they are strong enough to become unstable and create new vortices.^{20–23} Reference 24 showed that this was true for relatively short structures in the buffer layer, in the sense that inhibiting either the streaks or the vortices results in the decay of the other branch of the cycle.

However, some issues remain open. It is known that the instability of the streaks is a fast process that destroys them, after which new streaks take a relatively long time to reform,²⁵ and it is unclear how the vortices are maintained over the latency period in which the streaks are still too weak to become unstable again. Correspondingly, Ref. 26 noted that streaks strong enough to be unstable are relatively rare in the buffer layer, and proposed a transient model for the growth of the vortices that is much closer to the Orr mechanism than to a modal instability. Moreover, Ref. 27 showed that the dynamics of the cycle does not hold for near-wall structures longer than about 10^3 wall units, for which the relation of the two types of structures is hierarchical: damping the vortices damps the streaks, but damping the streaks does not damp the vortices. As far as we are aware, the matter has never been tested above the buffer layer, although it is known that an intermittent cycle similar to the one near the wall is present in the logarithmic region.²⁸ If we admit that the lift-up is the main contributor to the formation of streamwise-velocity streaks, the question posed in the title of this paper is how much can Orr's mechanism be considered responsible for the dynamics of the cross-plane velocities in wall-bounded turbulence.

The question has been addressed in the past, specially in meteorology, but mostly in a linear context linked to transition, to the formation of large-scale atmospheric waves.^{29–31} or to the generation of gravity waves in stratified flows.³² We are more interested here in whether a similar process can be invoked in fully nonlinear turbulent flows.

Since the perturbation energy associated with the Orr mechanism is transient, even in the inviscid limit, we will be led to consider intermittent flow events that we will denote as “bursts.” That term was originally introduced in turbulence to describe the fluid eruptions observed near the wall in the early visualizations of turbulent boundary layers,^{18,20} which were hypothesized to be reflections of the occasional break-up of the near-wall streaks mentioned above. However, even the original authors later acknowledged that the visualizations could be consistent with permanent advecting objects,³³ and the term eventually became associated with the ejections observed by stationary velocity probes. When numerical simulations showed that the streaks were long-lived streamwise velocity structures, and that the sweeps and ejections identified in the analysis of single-point data were mostly due to the passing of shorter quasi-streamwise vortices, intermittent in space but not necessarily in time,³⁴ the question of whether the observed temporally intermittent sublayer events were visualization artifacts or really existed in the near-wall layer was temporarily abandoned.

Although it has only recently become possible to follow individual turbulent structures for times long enough to distinguish between the two alternatives,³⁵ minimal and otherwise simplified simulations showed very early that there were temporally transient events in near-wall turbulence, with time scales substantially longer than the streak breakdown.^{21,24,36} They were originally denoted as “blooming,”²¹ to avoid the controversies current at the time, but the term did not catch. More recently, as experimental and simulation advances have eroded the reliance of turbulence research on

one-point measurements, the need for a special name for vortex passing has become less pressing, and “bursting” has began to be used again for intrinsically transient energetic events in shear turbulence.^{25,28,37–39} It is in that sense that it is used here.

The organization of the paper is as follows. The linear theory for the Orr mechanism in a uniform shear is reviewed and extended to turbulent-channel profiles in Sec. II. The evidence for transient bursting in minimal logarithmic-layer turbulence is analyzed and compared with the linear results in Sec. III, followed by an explicit analysis of the influence of nonlinearity in Sec. IV. Finally, the results are discussed and conclusions offered in Sec. V.

II. THE LINEARIZED PROBLEM

A. The equations of motion

The incompressible Navier–Stokes equations for a parallel shear flow can be written as

$$\partial_t u_i = N_i = -(U_j + u_j)\partial_j(U_i + u_i) - \partial_i(P + p) + \nu\partial_{jj}(U_i + u_i), \quad (1)$$

where capitals denote averages, $\langle \rangle$, defined with respect to the two “horizontal” directions (x_1, x_3) and time, lower-case symbols are fluctuations with respect to those means, repeated indices denote summation over 1 . . . 3, and the density is absorbed into the kinematic pressure p . The only non-zero mean quantities are $U \equiv U_1(x_2)$ and $P(x_1)$. The continuity equation is

$$\partial_i u_i = 0. \quad (2)$$

For parallel flows, the linearized version of (1) is

$$\partial_t u_i = L_i = -U\partial_1 u_i - u_2 U' \delta_i^1 - \partial_i p_L + \nu\partial_{jj} u_i, \quad (3)$$

where primed capitals denote derivatives with respect to x_2 , and δ_i^j is Kronecker’s delta. It can be reworked⁴⁰ into the Orr–Sommerfeld equation for the vertical velocity,

$$\partial_t \phi = -U\partial_1 \phi + U''\partial_1 u_2 + \nu\partial_{jj} \phi, \quad (4)$$

where $\phi = \nabla^2 u_2$, and the Squires equation for the vertical component of the vorticity,

$$\partial_t \omega_2 = -U\partial_1 \omega_2 - U'\partial_3 u_2 + \nu\partial_{jj} \omega_2. \quad (5)$$

From (2) and (3), the linearized pressure satisfies

$$\partial_{jj} p_L = -2U'\partial_1 u_2. \quad (6)$$

There is a similar Poisson’s equation for the full pressure in (1),

$$\partial_{jj} p = -2U'\partial_1 u_2 - (\partial_i u_j)(\partial_j u_i), \quad (7)$$

but the “fast” pressure p_L is generally different from p .⁴¹ The structure of these equations has been discussed often.¹⁵ The Orr–Sommerfeld equation is autonomous in u_2 , although continuity comes into it through the Laplacian in the definition of ϕ . This is easily seen from its derivation. Disregarding viscosity, the linearized equation for u_2 is

$$\partial_t u_2 + U\partial_1 u_2 = -\partial_2 p_L. \quad (8)$$

If we had also disregarded the pressure gradient, the only effect of (8) would be to tilt the perturbations with the shear, but not to change their amplitudes. Any amplification has to come from $\partial_2 p_L$. This is taken into account in the Orr–Sommerfeld equation by taking the Laplacian of (8), and substituting (6) into the right-hand side.

The Squires equation (5) is forced by the spanwise derivative of u_2 , which deforms the mean shear U' . Note that the Orr–Sommerfeld equation (4) has its own lift-up term, which creates vorticity fluctuations by deforming the mean vorticity gradient U'' , but we will see below that continuity, and not this term, is often the main mechanism for fluctuation growth. The solutions of (4) are usually associated with the Orr mechanism, and those of (5) with the lift-up, but the two are difficult to separate because they are coupled by the continuity constraint.

B. Inviscid homogeneous shear flow

Although all solutions to (1)–(3) are eventually modified by viscosity, or, in the case of turbulent flows, by some variant of an eddy dissipation,⁹ we have argued in the introduction that only processes with inviscid time scales are fast enough to be important in fully turbulent flows. Therefore, it is interesting to study the solutions of (3) in the limit $\nu = 0$. The simplest case is homogeneous shear flow, for which $U = Sx_2$. If we consider perturbations of the form $u_j = \hat{u}_j \exp(i\alpha_k x_k)$, and choose as the origin of time the moment when the wavefronts are vertical, the two wavenumbers α_1 and α_3 remain constant, and $\alpha_2 = -S\alpha_1 t$ varies as the perturbation is tilted forward by the shear.^{16,42} The three velocity components satisfy

$$\partial_t \hat{u}_1 = \frac{\alpha_1^2 - \alpha_3^2 - \alpha_2^2}{\alpha^2} S \hat{u}_2 - \nu \alpha^2 \hat{u}_1, \quad (9)$$

$$\partial_t \hat{u}_2 = \frac{2\alpha_1 \alpha_2}{\alpha^2} S \hat{u}_2 - \nu \alpha^2 \hat{u}_2, \quad (10)$$

$$\partial_t \hat{u}_3 = \frac{2\alpha_1 \alpha_3}{\alpha^2} S \hat{u}_2 - \nu \alpha^2 \hat{u}_3, \quad (11)$$

where $\alpha^2 = \alpha_0^2 + S^2 \alpha_1^2 t^2$ with $\alpha_0^2 = \alpha_1^2 + \alpha_3^2$. They can be expressed in terms of the dimensionless variables,

$$\hat{v}_j = \hat{u}_j(t) / \hat{u}_2(0); \quad \gamma_j = \alpha_j / \alpha_0; \quad \tau = -\gamma_2 = S\gamma_1 t; \quad Re = S\gamma_1 / \nu \alpha_0^2. \quad (12)$$

The inviscid solutions for $Re = \infty$ are

$$\hat{v}_1 = \gamma_1 \hat{v}_2 \tau - \frac{\gamma_3^2}{\gamma_1} \psi + \hat{v}_{10}, \quad (13)$$

$$\hat{v}_2 = \frac{1}{1 + \tau^2}, \quad (14)$$

$$\hat{v}_3 = \gamma_3 (\hat{v}_2 \tau + \psi) + \hat{v}_{30}, \quad (15)$$

$$\frac{\alpha_0 \hat{p}}{S \hat{u}_2(0)} = 2i\gamma_1 \hat{v}_2^2, \quad (16)$$

where the tilting angle with respect to the negative (α_1, α_3) direction,

$$\psi = \pi/2 + \arctan(\tau), \quad (17)$$

rotates from $\psi = 0$ at $t = -\infty$ to $\psi = \pi$ at $t = \infty$, and continuity requires that the perturbation at $t = -\infty$ satisfies $\hat{v}_{10}\gamma_1 + \hat{v}_{30}\gamma_3 = 0$.⁴² Since $\gamma_1^2 + \gamma_3^2 = 1$, the only parameter in (13)–(15) is γ_1 , which is the aspect ratio of the perturbation in the horizontal (x_1, x_3) plane. It ranges from $\gamma_1 = 0$ for perturbations which are infinitely long in the streamwise direction, to $\gamma_1 = 1$ for those that are purely spanwise. In the particular case of purely spanwise structures, ψ is the tilting angle with respect to $-x_1$.

Reference 43 treats the viscous problem (9)–(11) as one of the optimum amplification of initial conditions, but that concept is meaningless in the inviscid case. The non-zero initial conditions, \hat{v}_{10} and \hat{v}_{30} , are not modified by the shear, and the rest of the solution develops entirely from zero amplitude at $t = -\infty$. Disregarding any initial perturbation of the two horizontal velocities, \hat{v}_2 grows from $\hat{v}_2(-\infty) = 0$ to $\hat{v}_2(0) = 1$ and decays again to zero at $t = \infty$, but its cumulative effect is to generate non-zero perturbations for the other two velocity components that survive at $t = \infty$ except for purely spanwise waves with $\gamma_3 = 0$.

The vorticity lift-up term in (4) vanishes for this flow, because the mean shear is uniform, and one could expect the part of the flow due to (4), which reduces in that case to the effect of pressure on the tilting wavefronts, to be mostly potential. That is not exactly true. It turns out that even vanishingly small initial velocity perturbations need to have some wall-parallel vorticity to give rise

to a burst, because the infinitely large vertical wavenumber $\alpha_2 = \infty$ implies finite cross-stream gradients. Even so, the first terms in the right-hand sides of (13)–(15) do not create new vorticity, and can be considered as the irrotational Orr effect, while the terms proportional to the tilt angle grow monotonically with time, and represent the velocity lift-up.⁴³

The Orr burst of u_2 is an autonomous solution for which the effect of non-zero initial conditions $(\widehat{u}_2, \gamma_2)$ is only a rescaling and a shift in time, but its interaction with the pre-existing flow depends on the additive contributions \widehat{u}_{10} and \widehat{u}_{30} . In general, \widehat{u}_2 is very effective in harvesting energy from the mean shear into the other two velocity components, but whether that energy reinforces or damps existing perturbations depend on their relative geometry. For example, the normalized energy in \widehat{v}_1 tends to

$$|\widehat{v}_1|^2 = (\pi\gamma_3^2/\gamma_1)^2 + |\widehat{v}_{10}|^2 - 2(\pi\gamma_3^2/\gamma_1)|\widehat{v}_{10}|\cos(\theta), \quad (18)$$

for very long times, where θ is the phase angle of the complex initial condition, $\widehat{v}_{10} = |\widehat{v}_{10}|\exp(i\theta)$, when normalized with $\widehat{u}_2(0)$. If θ is assumed to be random in a turbulent flow, the last term in (18) can be positive or negative, and cancels on the average. On the other hand, the first term is always positive, and the net averaged effect of Orr bursts is to add energy to the two horizontal velocities. The amplification factor $(\pi\gamma_3^2/\gamma_1)^2$ can be large for streamwise elongated structures, for which $\gamma_1 \ll 1$. It is well known that, on average, energy in parallel shear flows is initially injected into u_1^2 by the interaction of the tangential Reynolds stress with the shear, and that the pressure-strain term redistributes it to the other two velocity components.⁴⁴ The details of the instantaneous interactions in an Orr burst are different. The pressure initially injects energy directly into u_2 , and indirectly into u_1 and u_3 . Those are the first terms in the right-hand sides of (13)–(15). At the same time, the lift-up transfers energy into u_1 , which in turn transfers some of it through pressure to u_3 . Those are the terms proportional to ψ . In the second part of the burst, the energy that had been injected by the pressure into u_2 flows back into the mean profile, although, because of the large amplification factor in the horizontal velocities, the total energy increases monotonically except for essentially spanwise perturbations ($\gamma_1 \gtrsim 0.9$). No energy remains in u_2 . Some examples of the inviscid evolution of selected aspect ratios are shown in Figure 3(a).

This exchange of energies can be seen more clearly in Figures 3(b) and 3(c), which plot the pressure terms in the energy equations for the individual velocity components, $\Pi_j = -u_j\partial_j p$, where no sum is intended on the repeated indexes. The corresponding Fourier coefficients are $\widehat{\Pi}_j = \alpha_j \text{Im}(\widehat{u}_j^* \widehat{p})$, where the asterisk denotes complex conjugation and $\text{Im}(\cdot)$ is the imaginary part. In Figure 3(b), which is drawn for equilateral perturbations with $\gamma_1 = \gamma_3 = 1/\sqrt{2}$, pressure initially injects energy into \widehat{u}_2 and \widehat{u}_3 , and draws it away from \widehat{u}_1 , although the energy in \widehat{u}_2 later flows back into the mean shear. It would appear from Figure 3(b) that the streamwise energy $|\widehat{u}_1|^2/2$, which is assumed to be initially zero, decreases and become negative, but the pressure is only part of the energy production term for that velocity component. The solid line with circles in the figure is the full production, which also includes the real part of $-\widehat{u}_1^* \widehat{u}_2$, and ensures that the energy stays positive. That the initial interaction of \widehat{u}_2 and \widehat{u}_1 is an autonomous property of the Orr–Sommerfeld equation is seen in Figure 3(c), which is drawn for two-dimensional spanwise perturbations with $\gamma_1 = 1$. Squires equation is inactive in this case, no spanwise velocity is created, and the energy given or taken away from \widehat{u}_2 is exactly compensated by the pressure term for \widehat{u}_1 . No long-term streak is generated, and the energy production for all the velocity components averages to zero over time, in spite of which the behavior of \widehat{u}_2 is exactly the same in both figures. The switch of sign in its production term is diagnostic for Orr bursts, and will be compared later with the observations of turbulent bursts in minimal boxes (Figure 6(d)).

At $t = \infty$, the two horizontal vorticity components become infinite in an inviscid flow, but viscosity damps those large gradients before they can develop. The viscous solutions to (9)–(11) are (13)–(15) multiplied by $\exp[-\tau(1 + \tau^2/3)/Re]$,⁴² which in practice limits the burst to $\tau \lesssim (3Re)^{1/3}$. If we interpret ν in a turbulent flow as representing turbulent dissipation, and assume that the resulting Reynolds number is $Re = 10 - 30$,⁴⁴ the limit should probably be taken as $\tau \lesssim 5$ for all but the most extreme wavenumber aspect ratios. Note that the tangential Reynolds stress, $-\widehat{u}_1 \widehat{u}_2^*$, is only active in $-5 \lesssim \tau \lesssim 5$, where $|\widehat{v}_2|$ is large, and that the final flow contains only horizontal

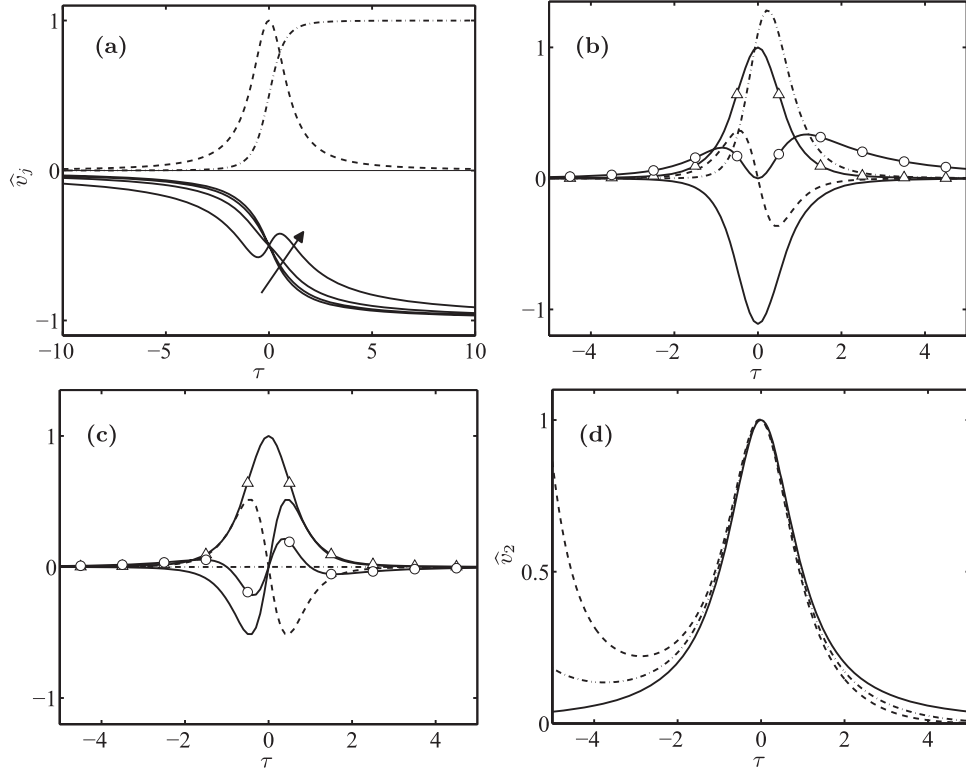


FIG. 3. (a) Normalized solutions of the linearized inviscid equations for a homogeneous shear flow. $\gamma_1 = 0.2(0.2)0.8$, increasing in the direction of the arrow. —, $\gamma_1 \hat{v}_1 / \gamma_3^2 \pi$; ---, \hat{v}_2 ; - · - · -, $\hat{v}_3 / \gamma_3 \pi$; (b) and (c) Terms from the energy equations for the individual velocity components, as defined in the text. Lines are pressure terms, normalized with $S|\hat{u}_{20}|^2$: —, $\hat{\Pi}_1$; ---, $\hat{\Pi}_2$; - · - · -, $\hat{\Pi}_3$; - ○ -, full streamwise energy production; -△-, $|\hat{v}_2|^2$, included as reference. (b) $\gamma_1 = 1/\sqrt{2}$. (c) $\gamma_1 = 1$. (d) Viscous solutions for \hat{v}_2 . —, $Re = \infty$; - · - · -, $Re = 30$; ---, $Re = 15$.

velocities and carries no tangential stress. The effect of viscosity on \hat{v}_2 is shown in Figure 3(d) for Reynolds numbers in the range mentioned above. The main difference with the inviscid case is that viscous solutions require non-zero initial conditions to survive, but their evolution during the active part of the burst changes little. Note also that, since the main effect of γ_1 is to change the effective Reynolds number, the relative insensitivity of the solutions to viscosity means that there is no strong viscous wavelength-selection mechanism, and that we can expect randomly initialized Orr solutions for u_2 to be essentially isotropic in the (x_1, x_3) plane.

C. The linear Orr mechanism in channels

The problem becomes more complicated in wall-bounded flows because the flow thickness introduces a length scale that cannot be absorbed into wavenumber ratios, and because the wall-parallel velocities cannot be analyzed without reference to the no-slip boundary condition or to viscosity. Nevertheless, since the Orr-Sommerfeld equation (4) is autonomous in u_2 and satisfies impermeability even in the inviscid limit, it is also possible in that case to identify an essentially inviscid Orr-like behavior for u_2 . In this section, we study a plane channel with a mean velocity profile mimicking turbulent channels parametrized by h^+ . The profile is derived by integrating the mean momentum equation $dU^+/dY = h^+(1 - Y)(\nu/\nu_t)$, where $Y = x_2/h$ and the total viscosity is⁶

$$\frac{\nu_t}{\nu} = \frac{1}{2} + \frac{1}{2} \left\{ 1 + \frac{\kappa^2 h^{+2}}{9} [2Y - Y^2]^2 [3 - 4Y + 2Y^2]^2 \left[1 - \exp\left(\frac{-x_2^+}{A}\right) \right]^2 \right\}^{1/2}, \quad (19)$$

with $\kappa' = 0.43$ and $A = 27.3$. That profile, with slightly different constants, was used in Ref. 9 to analyze the optimum transient growth of perturbations, using the eddy viscosity (19) in the perturbation equations. Here, since we are interested in approximating an inviscid behavior, we will maintain the profile and assume a constant viscosity ν_0 in the Orr-Sommerfeld equation, not necessarily equal to ν , to study the solutions in the limit of small ν_0 . The resulting perturbation equations are therefore formally inconsistent, and only make sense for phenomena whose lifetimes are short with respect to the evolution of the profile under the new viscosity. We will see below that the characteristic time for Orr bursts is approximately $1/U'$, where the shear is measured at some average location of the perturbation intensity profile. Denoting the latter by y_g , to be defined below, and centering on perturbations associated with the logarithmic layer, the viscous decay time for the profile at that wall distance is $O(y_g^2/\nu_0)$ which should be much slower than $1/U' = O(y_g/|u_\tau|)$. The consistency requirement is therefore that $y_g|u_\tau|/\nu_0 \gg 1$, which holds for perturbations peaking outside the buffer layer, especially if $\nu_0 \leq \nu$ (or, equivalently, if $h_0^+ = |u_\tau|/\nu_0 \geq h^+$).

The Orr-Sommerfeld equation for a single Fourier mode, $\phi = \widehat{\phi}(x_2) \exp[i(\alpha_1 x_1 + \alpha_3 x_3)]$, is

$$\partial_t \widehat{\phi} = i\alpha_1(-U\widehat{\phi} + U''\widehat{u}_2) + \nu_0(\partial_{22} - \alpha_0^2)\widehat{\phi}, \quad (20)$$

whose solutions can be made independent of α_1 by the Squire transformation that absorbs it into the reduced time $u_\tau \alpha_1 t$ and the Reynolds number $h_0^+ \gamma_1$.⁴⁰ The two remaining parameters are h^+ , which determines the mean velocity profile, and $\alpha_0 h$. We will scan values of $\alpha_0 h$ keeping the Reynolds number $\gamma_1 h_0^+$ constant for each scan, thus removing the direct effect of the aspect ratio γ_1 .

For each wavenumber, we search the most amplified perturbation using the method in Ref. 9, adapted from the programs in the Appendix of Ref. 15. However, in this case, the operator analyzed is only the Orr-Sommerfeld equation, and the energy maximized is that of the wall-normal velocity, $\|u_2\|^2 = h^{-1} \int_0^h |\widehat{u}_2|^2 dx_2$. In channels, because the mean profile is symmetric with respect to the centerline, the eigenfunctions of the linearized evolution equation can be classified into symmetric and antisymmetric. For all but the longest wavelengths, the eigenfunctions are localized near the walls and the two walls interact only weakly (see Figures 4(c) and 4(d)). As a consequence, eigenvalues come in almost degenerate pairs in which each eigenvalue is almost double, and so do the most amplified solutions. To remove that near-degeneracy, the analysis is done independently for perturbations which are even with respect to the channel centerline, $\widehat{u}_2(2h - x_2) = \widehat{u}_2(x_2)$, or odd, $\widehat{u}_2(2h - x_2) = -\widehat{u}_2(x_2)$. Two profiles are tested, with $h^+ = 1000$ and 2000 , using several numerical viscosities for each case. After some grid refinement tests, a uniform resolution of $N_T = 1024$ Tchebychev modes was used for all cases. With the exception of the very short wavelengths discussed below, there were no visible differences between computations from $N_T = 512$ to 1536 .

Generally speaking, \widehat{u}_2 behaves as in a homogeneous shear, evolving from a weak backwards-tilted perturbation to maximum amplitude when the phase front is roughly normal to the wall, and weakening again when the shear tilts it further forward. An example is shown in Figure 4(a) at five stages of its evolution, centered at the moment of maximum amplification. The perturbation has been normalized so that its imaginary part at maximum amplitude is as small as possible, and the fact that the Fourier eigenfunction at that moment can be made almost real shows that its phase fronts are essentially normal to the wall. The perturbation grows and decays over a time of the order of $u_\tau \alpha_1 t = 5$.

If we consider the Fourier coefficient of any quantity, such as $\widehat{u}_2 = |\widehat{u}_2| \exp(i\theta)$, the derivative $\partial_2 \theta$ represents a local vertical wavenumber, and a tilting angle equivalent to the one in (17) can be defined in terms of the imaginary part of $\widehat{u}_2^* \partial_2 \widehat{u}_2$,

$$\psi_2(x_2) = \pi/2 - \arctan(\partial_2 \theta / \alpha_0) = \pi/2 - \arctan\left(\frac{\text{Im} \frac{\widehat{u}_2^* \partial_2 \widehat{u}_2}{\alpha_0 |\widehat{u}_2|^2}}{\alpha_0 |\widehat{u}_2|^2}\right). \quad (21)$$

It is plotted in Figure 4(b) for the same cases as in Figure 4(a), and, even if there are obvious ambiguities near points where $|\widehat{u}_2| \approx 0$, the general trend is for the tilt to increase from zero at the early stages of the evolution towards $\psi_2 \approx \pi$ for large times, passing through $\psi_2 \approx \pi/2$ at the point of maximum amplification.

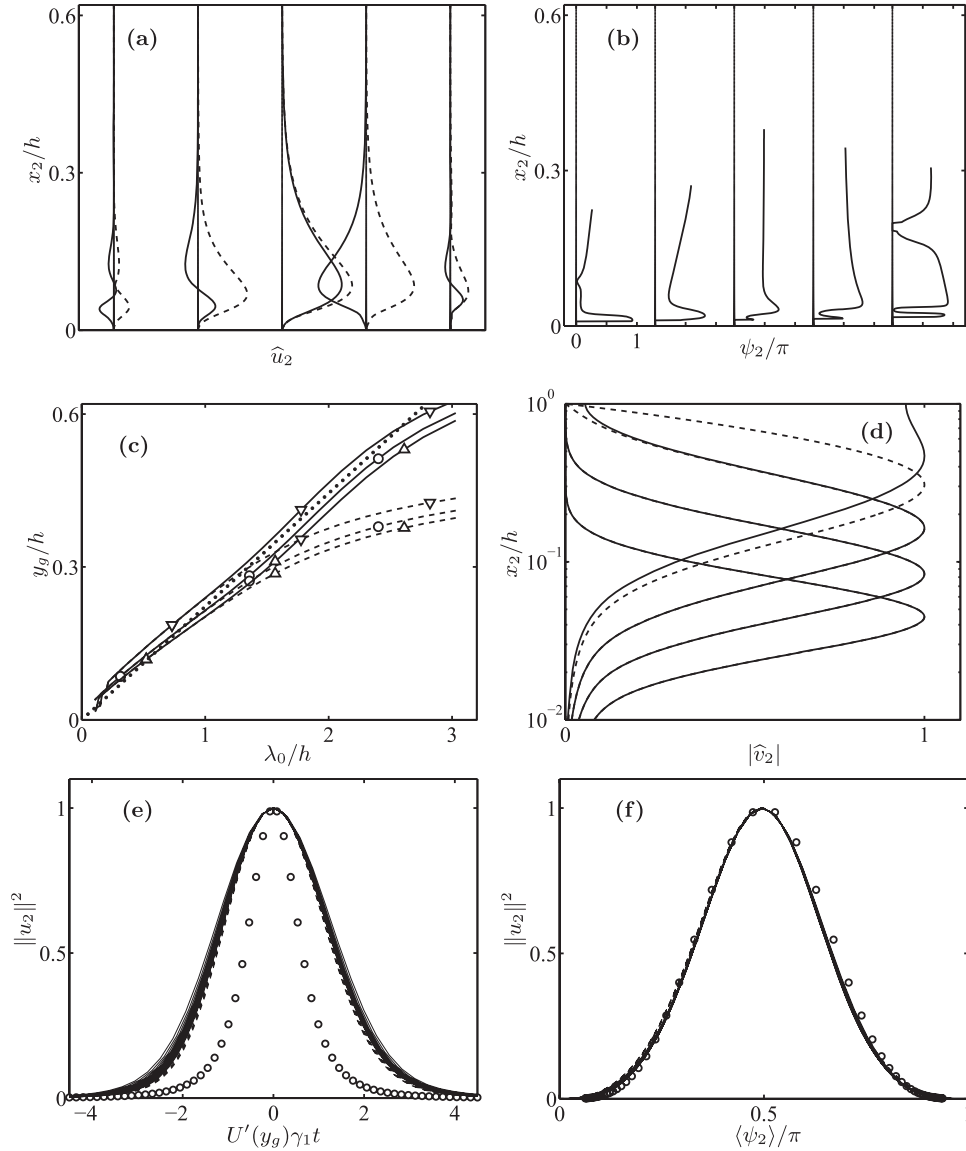


FIG. 4. Optimum-growth solutions for u_2 in channels with a turbulent mean profile. (a) Temporal evolution of an odd perturbation. $h^+ = 2000$, $h_0^+ = 9200$, $\lambda_0^+ = 980$. —, $\text{Re}(\hat{u}_2)$; ---, $|\hat{u}_2|$. Time is from left to right, separated between plots by $u_\tau \alpha_1 t = 0.95$, and centered on the moment of maximum amplification. (b) Tilting angle for the cases in (a), as defined in (21). (c) Center of gravity of the solutions at the moment of maximum amplification, as a function of λ_0 . —, Even \hat{u}_2 ; ---, odd. Δ , $h^+ = 2000$, $h_0^+ = 9200$; \circ , $h^+ = 2000$, $h_0^+ = 4600$; ∇ , $h^+ = 1000$, $h_0^+ = 2500$. The dotted line is $\lambda_0 = 4.5y_g$. (d) Modulus $|\hat{v}_2|$ of the solutions at maximum amplification. Cases as in (a), with λ_0^+ increasing from 390, 980, 2430, 6060, as solutions move away from wall. —, Even; ---, odd. (e) Temporal evolution of the energy of odd perturbations, against time scaled with the local shear and normalized to maximum amplitude. —, 15 wavelengths in $\lambda_0^+ = 890$ –2900 for $h^+ = 2000$, $h_0^+ = 9200$; ---, six wavelengths in $\lambda_0^+ = 890$ –1300 for $h^+ = 1000$, $h_0^+ = 2500$; \circ , homogeneous shear from (14). (f) As in (e), plotted as a function of the mean tilt.

If we define the instantaneous “height” of the perturbation as the position of its center of gravity,

$$x_{2g} = \int_0^h x_2 |\hat{u}_2|^2 dx_2 / \int_0^h |\hat{u}_2|^2 dx_2, \quad (22)$$

the solution moves slowly and irregularly away from wall, and we can define a characteristic height for each history as the height, y_g , at maximum amplification. For example, the case in Figures 4(a) and 4(b) move from $x_{2g} \approx 0.07$ to $x_{2g} \approx 0.12$, and is most amplified when $x_{2g} = y_g = 0.11$.

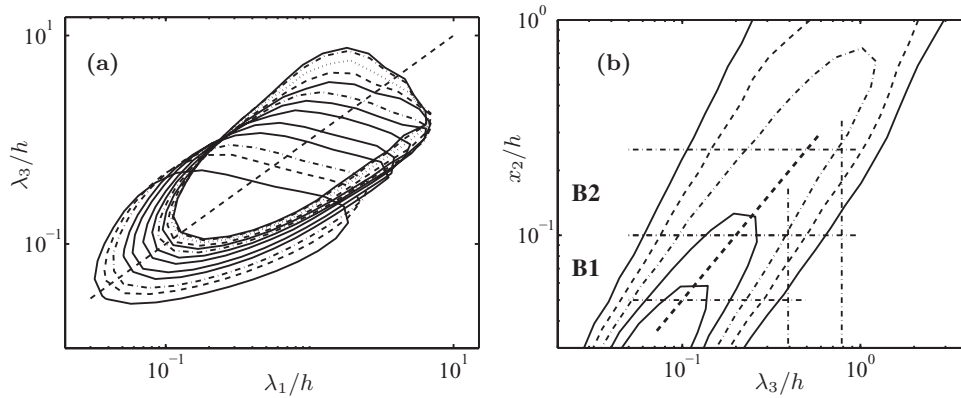


FIG. 5. (a) Premultiplied two-dimensional spectra of u_2 , as functions of λ_1 and λ_3 for $x_2/h = 0.05-1$ increasing towards the upper-right. Contours are $k_1 k_3 E_{22} = 0.04 u_2'^2$, and the dashed diagonal is $\lambda_1 = \lambda_3$. (b) Premultiplied one-dimensional spectrum of u_2 , versus λ_3 and x_2 . Contours are $k_3 E_{22} / u_2'^2 = 0.2(0.05)0.4$. The dashed diagonal is $\lambda_3 = 2x_2$. The two vertical lines are the widths of the channels N1800 and W1800 in Table I, and the horizontal ones are the limits of the respective averaging bands, as used in Figure 6. Both panels are channel C2000 in Table I.

Figure 4(b) shows that y_g grows linearly with $\lambda_0 = 2\pi/\alpha_0$, at least in the range $y_g^+ \gtrsim 100$, $y_g/h \lesssim 0.2$, which corresponds roughly to the conventional limits of the logarithmic layer in channels,³⁹ recalling the similar linear scaling of structures⁴⁵⁻⁴⁹ and spectra in wall-bounded flows (see Figure 5(b)). The linear behavior extends farther from the wall for even perturbations than for odd ones, clearly because the latter are constrained by the requirement that they should vanish at the centerline. The relation between y_g and λ_0 depends weakly on h^+ and h_0^+ , with a tendency to move closer to the wall with decreasing viscosity of either kind. The wavelengths associated with the linear behavior are in the range from $\lambda_0^+ \gtrsim 400$ to $\lambda_0/h \lesssim 1$. If we assume isotropy in the wall-parallel plane, and take y_g as the center of the u_2 structures, the wavelengths in Figure 4(c), $\lambda_3 \approx 6y_g$, are about twice wider than the ones given in the above-cited references for the structures in the logarithmic layer. However, note that the two quantities are not directly comparable, and that different structures have different widths. Moreover, it was noted in Ref. 27 that spectra tend to represent the distance between structures, rather than their sizes.

The relation between λ_0 and y_g is less clear below $y_g^+ = 100$, although that range is barely visible in Figure 4(c). The optimal solution oscillates there between two different types of initial conditions, depending on the computational parameters. One type continues smoothly the trends of the logarithmic layer, while the other one stays near $x_2^+ \approx 15$ during its full lifetime. Curiously, the difference between the two solutions does not seem to be a viscous effect. Each of them depends little on the viscosity ν_0 or on other numerical parameters, and it is only their relative amplifications that change. We have noted before that the Orr-Sommerfeld equation has its own lift-up term, proportional to U'' , which acts independently of the pressure effects responsible for the Orr bursts in homogeneous shear. This term is active in channels, but peaks sharply around $x_2^+ \approx 20$, and decays farther away from the wall,⁵⁰ suggesting the existence of two different bursting mechanisms in wall-bounded flows: one in the viscous layer, associated with the vorticity lift-up and presumably responsible for the peak of the kinetic energy at $x_2^+ \approx 15$ in wall turbulence,⁵¹ and a second one in the logarithmic layer, driven by pressure effects. The coexistence of the two mechanisms is restricted to wavelengths shorter than $\lambda_0^+ \approx 500$, and we will focus here on the longer outer solutions.

Figure 4(d) shows the modulus of the velocity eigenfunctions at maximum amplification, for four different wavelengths. For each case, the figure shows the even and odd eigenfunction, but they can only be distinguished for the two longest wavelengths, $\lambda_0 \approx h$ and $\lambda_0 \approx 3h$. Except for those two cases, both of which reach their maximum amplitudes well above the logarithmic layer, the perturbations at each wall behave independently from each other, and there is no difference between even and odd eigenfunctions. That is also clear in the heights in Figure 4(c).

Finally, Figure 4(e) shows the temporal evolution of the energy $\|u_2\|^2$. The discussion in Sec. II B suggests that the bursting time should be scaled with a characteristic shear felt by the perturbation, such as U' at y_g . That is done in Figure 4(e), which contains 21 different time histories from two profiles at different Reynolds numbers, with wavelengths ranging from $\lambda_0^+ \approx 850$ to $\lambda_0/h \approx 1.3$. The collapse is excellent, even if $U'(y_g)$ varies almost by a factor of 3 between the different curves in the figure. The figure also includes the solution (14) for homogeneous shear, which has the same general shape, but a time scale which is almost exactly twice faster. We can also define a tilting angle as an averaged version of (21),

$$\langle \psi_2 \rangle = \pi/2 - \arctan \left(\frac{\text{Im} \int_0^h \widehat{u}_2^* \partial_2 \widehat{u}_2 dx_2}{\alpha_0 \int_0^h |\widehat{u}_2|^2 dx_2} \right). \quad (23)$$

It grows smoothly from zero for negative times to π at positive ones, passing through $\pi/2$ at the moment of maximum amplification, strongly recalling the behavior for homogeneous flow. In fact, since the discussion in Sec. II B suggests that the tilting is the main reason behind the evolution of the velocity amplitudes, it is tempting to compare the two cases using ψ_2 as the evolution variable, instead of time. That is done in Figure 4(f), which contains all the cases in Figure 4(e). The collapse is even better than in the former figure, and includes the homogeneous case. There are no adjustable parameters in Figure 4(f), except perhaps the averaging used in (23) to define ψ_2 , but even that is probably not critical, since it is clear in Figure 4(b) that the tilt angle is relatively independent of x_2 .

The collapse in Figure 4(f) strongly supports the conclusion that all the cases in the figure are pressure-driven, and do not depend on the vorticity fluctuations generated by the lift-up Orr–Sommerfeld term. That term is missing from the homogeneous case, and that burst is fully due to the geometric deformation of the Laplacian in the definition of ϕ . That deformation is encoded in the tilt angle, and the excellent collapse of the two cases in terms of the tilt implies that any non-geometric effect present in the channel is also unimportant.

D. The wall parallel velocities

Analyzing the effect of the bursts on the other two velocity components requires considering Squire's equation (5),

$$\partial_t \widehat{\omega}_2 + i\alpha_1 U \widehat{\omega}_2 - \nu_0 (\partial_{22} - \alpha_0^2) \widehat{\omega}_2 = -iU' \alpha_3 \widehat{u}_2, \quad (24)$$

with homogeneous boundary conditions $\widehat{\omega}_2 = 0$ at the walls if $\nu_0 \neq 0$. The inviscid problem loses all the boundary conditions and can only be approximately analyzed away from the wall. Disregarding viscosity,

$$\widehat{\omega}_2(t) = \widehat{\omega}_{20} e^{-i\alpha_1 U t} - i\alpha_3 U' \int_0^t e^{i\alpha_1 U(\xi-t)} \widehat{u}_2(\xi) d\xi. \quad (25)$$

Two features of that solution are interesting because they recall similar behaviors in the homogeneous case. The first one is that the solution can be separated into initial conditions $\widehat{\omega}_{20}$, which are transported without amplification or decay, and a forced part in which \widehat{u}_2 injects energy into the flow independently of the initial conditions. As in the solution (18) for homogeneous shear, the second part is proportional to α_3 , and is strongest for streamwise oriented structures, but whether the result is an increase or a decrease of the total kinetic energy depends on the relative phases of the \widehat{u}_2 burst and the initial condition $\widehat{\omega}_{20}$.

The second interesting similarity is that the effect of the burst on the wall-parallel velocities, \widehat{u}_1 and \widehat{u}_3 , can be separated into bursting and secular parts. Those two velocity components can be expressed in the usual manner as linear combinations of $\partial_2 \widehat{u}_2$ and $\widehat{\omega}_2$.⁵¹ The part proportional to $\partial_2 \widehat{u}_2$ follows the growth and decay of the burst, and only the second one, represented by the integral in (25), has a long-term effect. Those two contributions correspond to the terms proportional to $\widehat{v}_2 \tau$ and ψ in the constant-shear solutions (13)–(15).

TABLE I. Numerical channels used in the text. The time T is used to compute the correlations.

Case	L_1/h	L_3/h	h^+	$u_\tau T/h$	Reference
C950	8π	3π	934		52
C2000	8π	3π	2003		53
W950	$\pi/2$	$\pi/4$	950	77.2	Present
N1800	$\pi/4$	$\pi/8$	1700	29.1	28
W1800	$\pi/2$	$\pi/4$	1840	41.3	28

III. BURSTING IN MINIMAL BOXES

While it is possible to study the temporal evolution of individual structures in full-size simulations,³⁵ it is much easier to do it in minimal boxes, which essentially contain a single structure, and which have been shown to reproduce well the statistics of full-size turbulence in the buffer²¹ and logarithmic layers.²⁸ In such computational boxes, structures can be studied in terms of integral quantities averaged over suitably chosen flow subdomains, avoiding the need to track them and the ambiguities between the Lagrangian and Eulerian points of view.

The simulations used in the rest of this paper are summarized in Table I. The reference data are from the turbulent channels C950⁵² and C2000,⁵³ computed in large doubly periodic boxes with streamwise and spanwise periodicities L_1 and L_3 . A full description of the simulations can be found in the respective original publications. The primary minimal box is W1800, with $h^+ = 1840$, which is minimal with respect to u_2 in $x_2/h \approx 0.1-0.5$. It was shown in Ref. 28 that wall turbulence remains “natural” as long as $x_2 \lesssim L_3/3$, corresponding to $x_2/h \lesssim 0.25$ in this case. The reason is seen in Figure 5, which displays spectra of u_2 in the larger channel C2000. Figure 5(a) shows that the spectra are roughly isotropic in the (x_1, x_3) plane, suggesting that any comparison with the theory in Secs. II A–II D should use $\gamma_1 = \gamma_3 = \lambda_0/\lambda_3 = 1/\sqrt{2}$. Figure 5(b) shows that the wavelengths of the spectra grow linearly as $\lambda_3 \approx 2x_2$. For $x_2 \ll L_3/2$, the active scales are much smaller than the box, and turbulence behaves as in a large box. For $x_2 \gtrsim L_3/2$, the core of the spectrum moves out of the box, and none of the energy-containing scales fit in the computational domain. In between those limits, the box is minimal for u_2 , and approximately contains a single large structure that can be studied by means of integrated quantities.

We therefore study the temporal evolution of flow variables integrated over such minimal boxes. For example, $[u_2^2]$ is computed by first defining fluctuations of u_2 with respect to their long-term averages at each x_2 , and averaging their squares over a band of x_2 and over the whole wall-parallel simulation domain. The band considered in the case of W1800 is $x_2/h = 0.1 - 0.25$, centered on $x_{2b}/h = 0.175$, and is denoted by B2 in Figure 5(b). Two more simulations were used to determine scaling. One is the narrower box N1800, at the same nominal Reynolds number as W1800, which is averaged over the lower band B1 between $x_2/h = 0.05 - 0.1$ ($x_{2b}/h = 0.075$), and the other, W950, is a lower-Reynolds number case in the same box as W1800, averaged over B2. The first two of those channels are the ones used in Ref. 28, extended here to longer times to improve statistics, while the last one was run for this paper using the same numerical code. Two sample traces of the band averages of the tangential stress and of the wall-normal energy are shown in Figure 6(a). The correlation of the two variables is striking, suggesting that there is a cycle of intermittent events involving more than one individual variable.

The evolution of each variable, and the relationships among them, can be studied by means of temporal correlations, defined for any two variables a and b as

$$C(a, b; t) = \frac{\langle [a(s)][b(s+t)] \rangle_s}{(\langle [a]^2 \rangle_s \langle [b]^2 \rangle_s)^{1/2}}, \quad (26)$$

where the average $\langle \rangle_s$ is taken over time and over the two sides of the channel.

The temporal autocorrelation function of $[u_2^2]$ is shown in Figure 6(b) for the three minimal boxes. They agree very well when the time is normalized with the mean shear over each box, and also agree tolerably well with the correlation computed from the linear Orr solution in Figure 4(e).

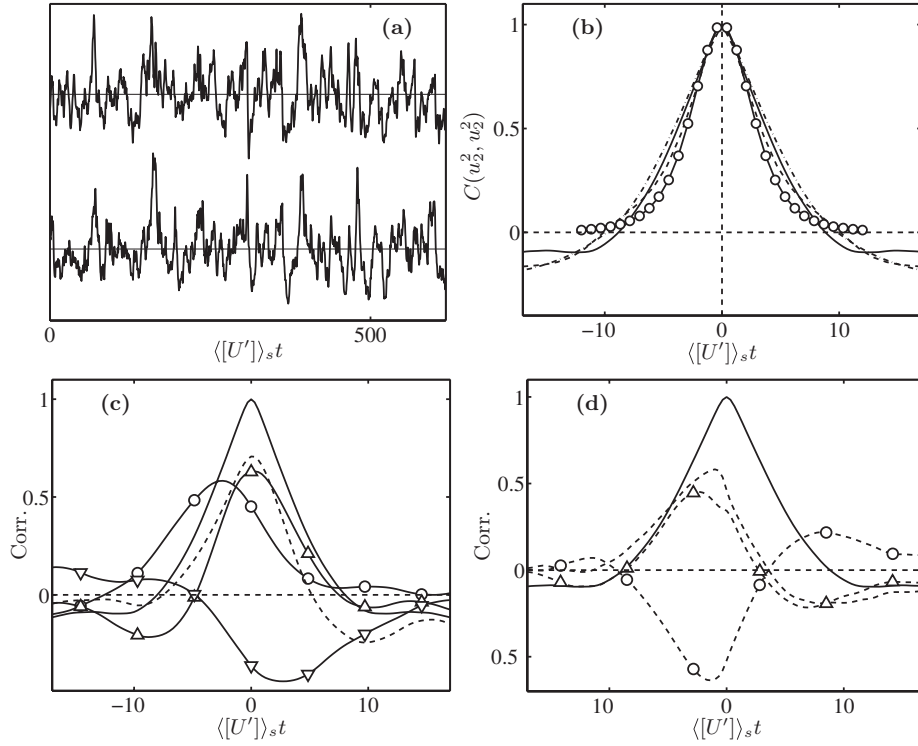


FIG. 6. (a) Sample time traces of $-[uv]$ on top, and $[v^2]$ at bottom, averaged over band B2 of W1800. (b) Temporal autocorrelation function of $[u_2^2]$. Time is scaled with the shear, averaged over the respective bands. —, W1800 in B2; $-\cdot-\cdot-$, N1800 in B1; $---$, W950 in B2; $-\circ-$, linearized solution from Figure 4(e), using $\gamma_1 = 1/\sqrt{2}$. (c) Temporal cross-correlations during a u_2 burst. W1800 in B2. —, $C(u_2^2, u_2^2)$; $-\circ-$, $C(u_2^2, u_1^2)$; $-\Delta-$, $C(u_2^2, u_3^2)$; $---$, $C(u_2^2, \varepsilon)$; $-\nabla-$, $C(u_2^2, \partial_2 U)$. (d) Cross-correlations with the pressure-strain energy fluxes. W1800 in B2. —, $C(u_2^2, u_2^2)$; $-\circ-$, $C(u_2^2, -u_1 \partial_1 p)$; $---$, $C(u_2^2, -u_2 \partial_2 p)$; $-\Delta-$, $C(u_2^2, -u_3 \partial_3 p)$.

Figures 6(c) and 6(d) show the temporal correlations of the different variables during a burst of u_2 . Figure 6(c) repeats the autocorrelation of $[u_2^2]$, and adds the cross-correlation of $[u_2^2]$ with the other two velocity components and with the energy dissipation rate ε . The streamwise velocity leads the maximum of $[u_2^2]$ by a few shear times, while the spanwise fluctuations, even if almost coincident with u_2 , are skewed towards later times, suggesting that the causality is from u_1 to u_2 to u_3 . The dissipation tracks u_2 fairly closely, but while u_3 dips before the burst, the dissipation dips after it, suggesting that the burst quiets the flow. The final correlation is of $[u_2^2]$ with the shear of the mean profile, $[\partial_2 u_1]$. Those two quantities are initially almost uncorrelated, but the shear decreases strongly during the burst, stressing the role of the bursts in flattening the mean velocity profile.

Figure 6(d) displays the temporal structure of the energy exchanges due to pressure among the different velocity components. We have already mentioned that the overall effect of pressure is to redistribute the energy among the different components, and that the overall flux is from the streamwise velocity to the other two. In fact, the balance outside the buffer layer of the two cross-stream velocities is almost exclusively between the pressure redistribution term and the dissipation. That is also true in minimal boxes. Figure 6(d) is keyed to the autocorrelation of $[u_2^2]$, and includes its cross-correlations with the pressure terms $[-u_j \partial_j p]$ that appear in the equations of the three kinetic-energy components $[u_j^2]/2$, and which were already discussed in Figures 3(b) and 3(c). Figure 6(d) represents the relative intensities of the energy exchanges due to pressure among components, but note that it should not be read as an energy balance. The correlations in the figure are computed after removing the long-term averages of the different quantities, and negative or positive correlations have to be interpreted as relative to those means. For example, when the time series for $[-u_1 \partial_1 p]$

is plotted directly, it is always negative, showing that the integrated role of u_1 is always to export energy to the other components. Correspondingly, $[u_2 \partial_2 p]$ and $[u_3 \partial_3 p]$ are always positive, showing that, when integrated over the box, they always receive energy from u_1 . What Figure 6(d) shows is that u_2 and u_1 partially reverse roles during the later part of the burst, and that some energy flows back from the former into the latter. That should be compared to the histories in Figures 3(b) and 3(c), and was mentioned in Sec. II B as one of the diagnostic features of the Orr mechanism.

A final question is whether it is possible to trace in the minimal boxes the tilting evolution observed in the linearized solutions. Unfortunately, it is not easy. The inclination angles can easily be computed by a suitably averaged version of the definition in (23), which can then be related to the inclination of the short-distance contours of the two-point spatial autocorrelation functions of the three velocity components. The time series of those three inclination angles are highly correlated with each other, with correlation coefficients between 0.75 and 0.9, suggesting that they represent properties of a common structure. They are also correlated with the bursts, with correlation coefficients with the velocities of the order of 0.5–0.6 at the top of the velocity temporal autocorrelation peaks, especially for u_1 and u_2 . Unfortunately, except within the buffer layer, they oscillate relatively little, and stay at values only slightly tilted forward from the vertical, making it difficult to conclude much about their evolution. The reason is that local angles measure the geometry over short distances of the smaller structures, of which there are many even in a minimal box. Any average is therefore most probably near zero, which corresponds to a vertical orientation. Even so, it is probably relevant that the angle closest to the vertical is the one for the wall-normal velocity, $\langle \psi_2 \rangle = 92^\circ$, while the other two velocity components are more inclined, $\langle \psi_1 \rangle = 99^\circ$ and $\langle \psi_3 \rangle = 103^\circ$. Over longer distances, it is known that the correlations of u_1 tend to be long, those of u_2 tall, and those of u_3 wide,⁵⁴ in agreement with the behavior of the linear models above. The velocity correlation functions are energy-weighted averages that tend to represent the orientation of the strongest structures. We have seen that the wall-normal velocity is strongest when the structures are vertical, while the other two velocities keep growing, while they tilt forward. Moreover, the differences between the two wall-parallel velocities agree with the ratio between the lift-up contributions to u_1 and u_3 in (13)–(15), which is proportional to α_3/α_1 . The streamwise velocity would tend to be stronger for long structures with small α_1 , while the spanwise component would be stronger for wide ones with small α_3 .

IV. THE EFFECT OF NONLINEARITY

A. How linear is wall-bounded turbulence?

While we have seen in Secs. II and III many similarities between linearized solutions and the behavior of natural turbulence, the relative magnitudes of the linear and nonlinear terms in the equations of motion still have to be established directly in the natural case, particularly regarding the pressure terms that might be expected to contribute to Orr bursting.

The most straightforward way of doing so in full simulations is to compute the root-mean-squared (r.m.s.) magnitudes of the right-hand sides of the various equations, such as $N'^2 \equiv \langle N^2 \rangle$ in the full Navier–Stokes equation (1), or $L'^2 \equiv \langle L^2 \rangle$ in the linearized version (3). Those two accelerations are displayed as functions of x_2 in Figure 7(a), which shows that the full nonlinear acceleration N' has very nearly the same magnitude as the linearized right-hand side L' . Moreover, the magnitude of the difference $(N' - L')$ is much smaller than either of the two, showing that the agreement of the two quantities is not coincidental, and that the full acceleration N' is mostly linear.

Part of the reason is revealed in Figure 7(b), which shows semi-Lagrangian accelerations, such as $\tilde{N}_j = N_j + U \partial_1 u_j$, in which the effect of the advection by the mean flow has been removed. Both in the linear and in the nonlinear case, the residual accelerations are much weaker than those in Figure 7(a), showing that most of the linear contribution to the Eulerian acceleration is the advection by the mean flow. Moreover, in this case, the residual linearized terms are substantially smaller than the nonlinear ones, especially above the buffer layer. It turns out (not shown) that most of the linear semi-Lagrangian acceleration is viscous, $\nu \nabla^2 u$, while the r.m.s. magnitude of the pressure gradient, ∇p , which is part of \tilde{N} , is almost equal to \tilde{N}' . The different magnitudes of \tilde{L}' and \tilde{N}' in Figure 7(b)

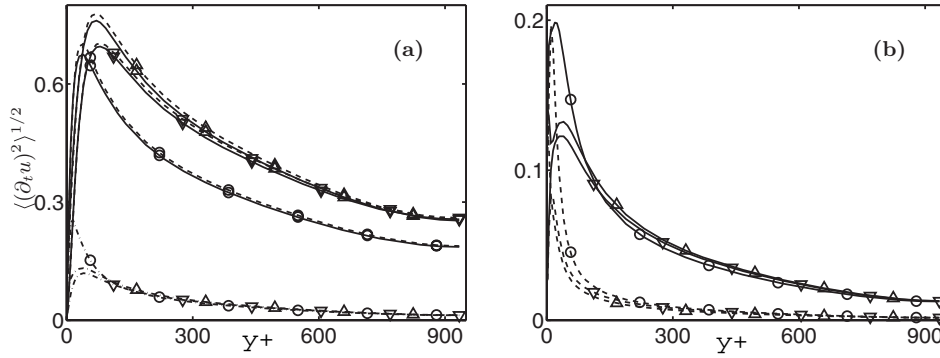


FIG. 7. Root-mean-squared accelerations for channel C950, scaled in wall units. (a) Eulerian: —, fully nonlinear N in (1); ---, linear L in (3); - · - · -, $|N - L|$. (b) Semi-Lagrangian: —, $\tilde{N} = N + U \partial_t u$; ---, $\tilde{L} = L + U \partial_t u$. Symbols represent velocity components: \circ , u_1 ; ∇ , u_2 ; Δ , u_3 .

are therefore consistent with the known result that the pressure terms dominate the viscous ones in the Lagrangian accelerations in isotropic turbulence,⁵⁵ and also with the observation that the fast pressure p_L is a relatively small part of the total one.^{41,56} However, the magnitude of the terms in which the acceleration can be decomposed is not additive, because the terms are not necessarily uncorrelated. Thus, while it can be concluded from the previous discussion that the much smaller viscous term is not an important part of \tilde{N} , the only reason why N and L can be claimed from Figure 7(a) to be almost equal is that the magnitude of their difference is independently checked to be small. The same is not true for \tilde{N} and the pressure gradient. The fact that their r.m.s. magnitudes are similar does not imply that the nonlinear advective term, $-u \nabla u$, which is the remaining part of \tilde{N} , is negligible. In fact, if we neglect viscosity, $-\nabla p$ is the full Lagrangian acceleration $(\partial_t + u \nabla)u$, while $\tilde{N} = (\partial_t + U \partial_1)u$ is its Eulerian counterpart in the frame of reference of the mean flow. It is known from isotropic turbulence that the latter is typically much weaker than the former⁵⁷ because of the sweeping of the small scales by the larger ones, implying substantial cancellation between the two terms.

That the dominant semi-Lagrangian accelerations are nonlinear could have been expected *a priori* because they are small-scale quantities, but inspection of their spectra (not shown) reveals that, even if the difference between the linear and nonlinear terms becomes smaller for the larger scales, the nonlinear terms dominate everywhere, except for very wide structures of u_2 ($\lambda_2 \gtrsim h$), and for very long ones of u_1 ($\lambda_1 \gtrsim 5h$). The main conclusion from Figure 7(b) should be that any model in which linearized pressure is the dominant energy-injection mechanism for u_2 is incomplete.

Another interesting observation is that the magnitudes of the semi-Lagrangian accelerations in Figure 7(b) are similar for the three velocity components above the buffer layer, while the full acceleration for u_1 is substantially smaller than the other two in Figure 7(a). That makes sense for the pressure terms, which are isotropic, and for the viscous ones, which mostly involve small dissipative scales, but it is a little surprising for the advective terms, which include the lift-up contribution $u_2 U'$ in both \tilde{L}'_1 and \tilde{N}'_1 . The lower total acceleration of u_1 in Figure 7(a) can only be due to weaker streamwise gradients of that velocity component, even if the intensity of u_1 is the highest of the three.⁵¹ That is consistent with the longer streamwise dimensions of the u_1 spectra,^{52,56,58} but implies that part of the streamwise velocity is not only “inactive,” in the Townsend⁵⁹ sense of not carrying Reynolds stresses, but “passive” in the sense of evolving much more slowly than the other two velocity components.

B. A nonlinear Orr mechanism

Given the similarities discussed above between turbulent bursting and the linearized Orr burst, the realization that most of the acceleration beyond simple advection by the mean shear is nonlinear, even for the wall-normal velocity involved in the Orr mechanism, is a little puzzling. However, it is

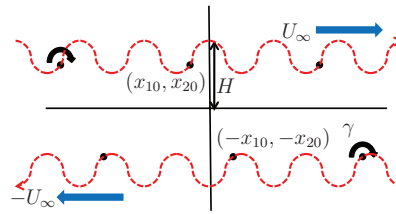


FIG. 8. Sketch of the vortex street analyzed in the text.

important to realize that the Orr mechanism is not intrinsically linear, even if it is contained in the linear approximation, and if it is easiest to analyze in a linear context.

In fact, it is easy to construct nonlinear Orr analogs. Consider the simple two-dimensional case sketched in Figure 8, in which two infinite rows of identical point vortices of circulation $\gamma = -\pi$ slide past each other. Disregarding instability issues, both rows move without internal deformation, while the inter-row distance changes as the vortices in the upper row slide relative to those in the lower one. If the pitch of each row is $\Delta x_1 = \pi$, so that the circulation per unit length of each row is unity, the velocity jump across the double vortex layer is $2U_\infty = 2$. Parametrize the problem by the distance $2H$ between the rows at the moment in which the vortices pass directly on top of each other, and the two rows are farthest apart. As the top row moves to the right and the bottom one to the left along the dashed wavy trajectories in Figure 8, they preserve symmetry about the origin, so that their positions can be fully described by the coordinates (x_{10}, x_{20}) of an arbitrary vortex in the upper row. This problem is a variant of the analysis of vortex streets in Ref. 60. Defining a complex variable, $z = x_1 + ix_2$, the velocity is given by

$$u_1 - iu_2 = \frac{i}{2} [\cot(z - z_0) + \cot(z + z_0)], \tag{27}$$

and the motion of the rows is governed by

$$\frac{dz_0^*}{dt} = \frac{i}{2} \cot(2z_0). \tag{28}$$

The total kinetic energy is conserved once self-interactions and the free streams are removed,⁶¹ but it is exchanged by the pressure between the two velocity components, as in the Orr mechanism. When $H \gg \pi$, the two rows interact weakly, and the problem can be considered linear. As it approaches the critical value $H = \log(1 + \sqrt{2})/2 \approx 0.44$,⁶² the interaction becomes more nonlinear and the distance between the rows oscillates strongly. Below that limit, the two rows stop sliding, and the vortices rotate around each other in pairs. Three sample trajectories are given in Figure 9(a), spanning those limits.

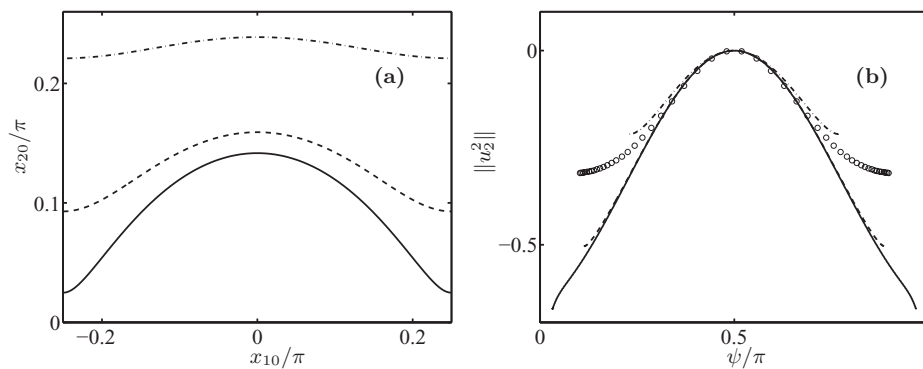


FIG. 9. (a) Trajectories of a vortex in the upper row of the model problem in Figure 8, as it moves from left to right. (b) Time evolution of the energy of the vertical velocity, versus the relative angle between the vortices. Lines are different row separations: —, $H = 0.445$; ---, $H = 0.5$; - · - · -, $H = 0.75$; \circ , homogeneous shear.

As vortices pass on top of each other, their vertical velocities reinforce one another, and the integrated magnitude of $\|u_2^2\|$ has a maximum. At those moments, their horizontal velocities tend to cancel, and $\|u_1^2\|$ has a minimum. The opposite is true when the vortices are maximally staggered, as shown in Figure 9(b). It is difficult in this case to define an appropriate mean shear with which to normalize time, because the mean velocity profile is formed by two sharp steps at the average position of the rows, but it follows from the previous discussions of the Orr bursts that the relevant variable is the inclination angle of the flow features, which can be defined here as the angle $\psi = \pi/2 + \arctan(x_{20}/x_{10})$ between neighboring vortices in opposite rows. The three energy histories in Figure 9(b) are plotted against that angle, which does not span the full range $\psi = (0, \pi)$ in this periodic problem. They collapse well over their respective ranges. The figure also includes the burst (14) in a homogeneous-shear, plotted against the inclination angle of the wavefronts. It also agrees reasonably well, although that particular agreement should not be taken too seriously. Although it shows that the temporal scale, measured in terms of the inclination angle, is of the same order of magnitude in both flows, the ambiguity appears in the scaling of $\|u_2^2\|$. There is no well-defined zero-energy level in the case of the double vortex row. The energies in the figure are given relative to their maxima, and scaled with U_∞^2 . Conversely, there is no scaling velocity in the homogeneous case, which has been plotted in the figure with the energy scaling resulting in the best fit with the point-vortex case. No adjustment has been made to the angles in the abscissas.

Note that this example, along with others that could be similarly constructed, does not question the linearity of the mechanism discussed in Sec. III. Rather, the implication is that the linearized version is a particular case of a more general nonlinear phenomenon in which the pressure redistributes energy between the different velocity components whenever two localized structures are carried past each other by the velocity differences in the sheared flow. The localization of the structures was represented in Sec. III by the wall-parallel periodicity, and in the case in this section by the vorticity concentration in the point vortices. In the present two-dimensional case, the energy exchange has no lasting effect, and the energy history is periodic in time. In the oblique cases in Sec. III (with $\gamma_3 \neq 0$) the burst of u_2 leaves in its wake a permanent streak of the wall-parallel velocity components.

V. DISCUSSION AND CONCLUSIONS

In summary, we have reviewed the classical theory of inviscid linearized Orr bursts in homogeneous shear flow, and extended it to channels with turbulent profiles. We have shown that both cases share similar dynamics for u_2 , at least above the buffer layer of the channel, strongly suggesting that the dominant effect in the channel is the pressure in the Orr–Sommerfeld equation, rather than the vorticity lift-up, since the latter is missing from the homogeneous shear. We have also observed that, since the wall-parallel aspect ratio of the fluctuations can be absorbed in the viscosity of the Orr–Sommerfeld equation, the inviscid character of the Orr mechanism implies that the spectrum of u_2 can be expected to be roughly isotropic in the horizontal plane. That is indeed the case in the logarithmic layer, in contrast to other velocity components. On the other hand, we have noted in passing that the mechanism very near the wall might be different. The second wall-normal derivative of the mean velocity is large in that region,⁵⁰ and the vorticity lift-up term of the Orr–Sommerfeld equation might become important. For example, one of the consequences of that term is that the flow can undergo a Kelvin–Helmholtz instability if U'' vanishes. That does not happen above the buffer layer, and is inhibited near the wall by the impermeability boundary condition but, if that condition is relaxed by porosity⁶³ or by other means,⁵⁰ the Kelvin–Helmholtz instability reappears, with vertical eigenfunctions that remain localized below $x_2^+ \approx 30$.^{50,64}

We have also analyzed the bursts in simulations of fully turbulent flows in computational boxes that are minimal with respect to the structures of the logarithmic layer. We have shown that they share many features with the linearized bursts, especially for the wall-normal velocity u_2 . For example, the wall-parallel dimensions of the structures grow linearly with the distance to the wall in both cases, and, when the temporal correlations of the logarithmic-layer bursts are normalized with the local shear of the mean velocity profile, their temporal scales agree well with the bursts in linearized channels. We have noted that shear scaling of the times is equivalent to the proportionality to the distance to the wall observed in previous studies.^{28,35} We have also shown that, during a

burst, the pressure-redistribution terms in the energy equation act partially in opposite directions to their normal ones. While, on the average, pressure in parallel shear flows exports energy from u_1 into the two cross-stream velocities, the opposite is true during the last part of the bursts, and u_2 exports energy into both u_1 and u_3 . The same is not true, for example, of the peaks of u_3^2 , and is a diagnostic characteristic of the Orr mechanism. Finally, although we have not been able to track the temporal evolution of the inclination angles of individual turbulent structures, we have shown that the linearized model is consistent with the known structure of the two-point correlation functions of the three velocity components.

Even so, we have argued that a linearized Orr explanation for the observed turbulent bursts cannot be complete, except in the sense that the main term in the equations of motion is overwhelmingly the tilting of the structures by the sheared mean profile. The classical model for the generation of the vortices in the buffer layer is that they result from the break-up of the streamwise velocity streaks,^{18,20} and there is ample evidence that the sequence of events in the bursts of the logarithmic layer resemble closely that near the wall.²⁸ In fact, the cross-correlations in Figure 6(c) clearly show that u_2^2 follows a previous maximum of u_1^2 . The inviscid Orr burst is autonomous, and develops over an infinite time from zero-energy initial conditions, but, in real dissipative flows, it has to be seeded. The best interpretation of the observations just discussed is that the Orr mechanism is the way in which the flow implements the growth of the wall-normal velocities initiated by the instabilities of the streamwise velocity streaks. The interesting point is that, since Orr bursts get their energy directly from the mean shear, they answer the question of how the vertical velocities are maintained and amplified even after the original streak has been destroyed. Their time scale, of the order of ten shear times, is long enough to provide a delay mechanism by which the flow can be reorganized after the streaks break down, and restarted after a while. The observed length of the bursting cycle, $Tu_\tau/x_2 \approx 6$,²⁸ equivalent to $U'T \approx 15$, is consistent with such a delay.

A second reason to reject strict linearity is that, when the accelerations in the flow are measured directly, they are found to be mostly nonlinear except for the dominant advection by the mean velocity. In particular, the effect of the linearized “fast” pressure is found to be weak with respect to the total pressure, in agreement with the relative magnitudes of the two pressure components.^{41,56} However, we have shown by a simple example that the Orr mechanism is not necessarily linear. It occurs whenever a vortical structure, whether weak or strong, overtakes another at a lower level of a shear flow, and their cross-shear velocities reinforce each other.

The implied model is that, as the streak breaks down, it injects vorticity into the flow, which is then amplified by the Orr mechanism into strong wall-normal velocities that eventually restart the streak.

ACKNOWLEDGMENTS

This work was supported by the European Research Council Grant No. ERC-2010.AdG-20100224. The careful critique by Dong Siwei of a previous version of this paper is gratefully acknowledged.

- ¹ A. N. Kolmogorov, “The local structure of turbulence in incompressible viscous fluids at very large Reynolds numbers,” *Dokl. Akad. Nauk SSSR* **30**, 301–305 (1941); reprinted in A. N. Kolmogorov, *Proc. R. Soc. London. A* **434**, 9–13 (1991).
- ² L. Keefe, P. Moin, and J. Kim, “The dimension of attractors underlying periodic turbulent Poiseuille flow,” *J. Fluid Mech.* **242**, 1–29 (1992).
- ³ G. L. Brown and A. Roshko, “On the density effects and large structure in turbulent mixing layers,” *J. Fluid Mech.* **64**, 775–816 (1974).
- ⁴ M. Gaster, E. Kit, and I. Wygnanski, “Large-scale structures in a forced turbulent mixing layer,” *J. Fluid Mech.* **150**, 23–39 (1985).
- ⁵ W. C. Reynolds and W. G. Tiederman, “Stability of turbulent channel flow, with application to Malkus’ theory,” *J. Fluid Mech.* **27**, 253–272 (1967).
- ⁶ A. K. M. F. Hussain and W. C. Reynolds, “The mechanics of an organized wave in turbulent shear flow,” *J. Fluid Mech.* **41**, 241–258 (1970).
- ⁷ W. V. R. Malkus, “Outline of a theory of turbulent shear flow,” *J. Fluid Mech.* **1**, 521–539 (1956).
- ⁸ K. M. Butler and B. F. Farrell, “Optimal perturbations and streak spacing in wall-bounded shear flow,” *Phys. Fluids A* **5**, 774–777 (1993).
- ⁹ J. C. del Álamo and J. Jiménez, “Linear energy amplification in turbulent channels,” *J. Fluid Mech.* **559**, 205–213 (2006).

- ¹⁰C. Cossu, G. Pujals, and S. Depardon, "Optimal transient growth and very large-scale structures in turbulent boundary layers," *J. Fluid Mech.* **619**, 79–94 (2009).
- ¹¹P. J. Schmid, "Nonmodal stability theory," *Annu. Rev. Fluid Mech.* **39**, 129–162 (2007).
- ¹²S. Corrsin, "Local isotropy in turbulent shear flow," NACA Research Memorandum 58B11, Washington, 1958.
- ¹³S. G. Saddoughi and S. V. Veeravali, "Local isotropy in turbulent boundary layers at high Reynolds numbers," *J. Fluid Mech.* **268**, 333–372 (1994).
- ¹⁴M. J. Lee, J. Kim, and P. Moin, "Structure of turbulence at high shear rates," *J. Fluid Mech.* **216**, 561–583 (1990).
- ¹⁵P. J. Schmid and D. S. Henningson, *Stability and Transition in Shear Flows* (Springer, 2001), pp. 55–58.
- ¹⁶W. M. Orr, "The stability or instability of the steady motions of a perfect liquid and of a viscous liquid. Part I: A perfect liquid," *Proc. R. Ir. Acad. A* **27**, 9–68 (1907), <http://www.jstor.org/stable/20490590>.
- ¹⁷T. Ellingsen and E. Palm, "Stability of linear flow," *Phys. Fluids* **18**, 487–488 (1975).
- ¹⁸S. J. Kline, W. C. Reynolds, F. A. Schraub, and P. W. Runstadler, "Structure of turbulent boundary layers," *J. Fluid Mech.* **30**, 741–773 (1967).
- ¹⁹J. D. Swearingen and R. F. Blackwelder, "The growth and breakdown of streamwise vortices in the presence of a wall," *J. Fluid Mech.* **182**, 255–290 (1987).
- ²⁰H. T. Kim, S. J. Kline, and W. C. Reynolds, "The production of turbulence near a smooth wall in a turbulent boundary layer," *J. Fluid Mech.* **50**, 133–160 (1971).
- ²¹J. Jiménez and P. Moin, "The minimal flow unit in near-wall turbulence," *J. Fluid Mech.* **225**, 213–240 (1991).
- ²²J. Jiménez, "On the structure and control of near wall turbulence," *Phys. Fluids* **6**, 944–953 (1994).
- ²³J. M. Hamilton, J. Kim, and F. Waleffe, "Regeneration mechanisms of near-wall turbulence structures," *J. Fluid Mech.* **287**, 317–248 (1995).
- ²⁴J. Jiménez and A. Pinelli, "The autonomous cycle of near wall turbulence," *J. Fluid Mech.* **389**, 335–359 (1999).
- ²⁵J. Jiménez, G. Kawahara, M. P. Simens, M. Nagata, and M. Shiba, "Characterization of near-wall turbulence in terms of equilibrium and 'bursting' solutions," *Phys. Fluids* **17**, 015105 (2005).
- ²⁶W. Schoppa and F. Hussain, "Coherent structure generation in near-wall turbulence," *J. Fluid Mech.* **453**, 57–108 (2002).
- ²⁷J. Jiménez, J. C. del Álamo, and O. Flores, "The large-scale dynamics of near-wall turbulence," *J. Fluid Mech.* **505**, 179–199 (2004).
- ²⁸O. Flores and J. Jiménez, "Hierarchy of minimal flow units in the logarithmic layer," *Phys. Fluids* **22**, 071704 (2010).
- ²⁹J. P. Boyd, "The continuous spectrum of linear Couette flow with the beta effect," *J. Atmos. Sci.* **40**, 2304–2308 (1983).
- ³⁰B. F. Farrell, "Developing disturbances in shear," *J. Atmos. Sci.* **44**, 2191–2199 (1987).
- ³¹B. F. Farrell and P. J. Ioannou, "Stochastic forcing of the linearized Navier–Stokes equations," *Phys. Fluids A* **5**, 2600–2609 (1993).
- ³²B. F. Farrell and P. J. Ioannou, "Transient development of perturbations in stratified shear flow," *J. Atmos. Sci.* **50**, 2201–2214 (1993).
- ³³G. R. Offen and S. J. Kline, "A proposed model for the bursting process in turbulent boundary layers," *J. Fluid Mech.* **70**, 209–228 (1975).
- ³⁴S. K. Robinson, "Coherent motions in the turbulent boundary layer," *Annu. Rev. Fluid Mech.* **23**, 601–639 (1991).
- ³⁵A. Lozano-Durán and J. Jiménez, "Time-resolved evolution of the wall-bounded vorticity cascade," *J. Phys.: Conf. Ser.* **318**, 062016 (2011).
- ³⁶J. Jiménez and M. P. Simens, "Low-dimensional dynamics in a turbulent wall flow," *J. Fluid Mech.* **435**, 81–91 (2001).
- ³⁷G. Kawahara and S. Kida, "Periodic motion embedded in plane Couette turbulence: Regeneration cycle and burst," *J. Fluid Mech.* **449**, 291–300 (2001).
- ³⁸G. Kawahara, M. Uhlmann, and L. van Veen, "The significance of simple invariant solutions in turbulent flows," *Annu. Rev. Fluid Mech.* **44**, 203–225 (2012).
- ³⁹J. Jiménez, "Cascades in wall-bounded turbulence," *Annu. Rev. Fluid Mech.* **44**, 27–45 (2012).
- ⁴⁰P. G. Drazin and W. H. Reid, *Hydrodynamic Stability* (Cambridge University Press, 1981).
- ⁴¹J. Kim, "On the structure of pressure fluctuations in simulated turbulent channel flow," *J. Fluid Mech.* **205**, 421–451 (1989).
- ⁴²A. A. Townsend, *The Structure of Turbulent Shear Flow*, 2nd ed. (Cambridge University Press, 1976), Chap. 3.12.
- ⁴³B. F. Farrell and P. J. Ioannou, "Optimal excitation of three-dimensional perturbations in viscous constant shear flow," *Phys. Fluids A* **5**, 1390–1400 (1993).
- ⁴⁴H. Tennekes and J. L. Lumley, *A First Course in Turbulence* (MIT Press, 1972).
- ⁴⁵H. Nakagawa and I. Nezu, "Structure of space-time correlations of bursting phenomena in an open channel flow," *J. Fluid Mech.* **104**, 1–43 (1981).
- ⁴⁶B. Ganapathisubramani, E. Longmire, and I. Marusic, "Characteristics of vortex packets in turbulent boundary layers," *J. Fluid Mech.* **478**, 35–46 (2003).
- ⁴⁷C. D. Tomkins and R. J. Adrian, "Spanwise structure and scale growth in turbulent boundary layers," *J. Fluid Mech.* **490**, 37–74 (2003).
- ⁴⁸J. C. del Álamo, J. Jiménez, P. Zandonade, and R. D. Moser, "Self-similar vortex clusters in the logarithmic region," *J. Fluid Mech.* **561**, 329–358 (2006).
- ⁴⁹A. Lozano-Durán, O. Flores, and J. Jiménez, "The three-dimensional structure of momentum transfer in turbulent channels," *J. Fluid Mech.* **694**, 100–130 (2012).
- ⁵⁰R. García-Mayoral and J. Jiménez, "Hydrodynamic stability and breakdown of the viscous regime over riblets," *J. Fluid Mech.* **678**, 317–347 (2011).
- ⁵¹J. Kim, P. Moin, and R. D. Moser, "Turbulence statistics in fully developed channel flow at low Reynolds number," *J. Fluid Mech.* **177**, 133–166 (1987).
- ⁵²J. C. del Álamo, J. Jiménez, P. Zandonade, and R. D. Moser, "Scaling of the energy spectra of turbulent channels," *J. Fluid Mech.* **500**, 135–144 (2004).

- ⁵³ S. Hoyas and J. Jiménez, “Scaling of the velocity fluctuations in turbulent channels up to $Re_\tau = 2003$,” *Phys. Fluids* **18**, 011702 (2006).
- ⁵⁴ J. Jiménez, S. Hoyas, M. P. Simens, and Y. Mizuno, “Turbulent boundary layers and channels at moderate Reynolds numbers,” *J. Fluid Mech.* **657**, 335–360 (2010).
- ⁵⁵ P. K. Yeung, S. B. Pope, A. G. Lamorgese, and D. A. Donzis, “Acceleration and dissipation statistics of numerically simulated isotropic turbulence,” *Phys. Fluids* **18**, 065103 (2006).
- ⁵⁶ J. Jiménez and S. Hoyas, “Turbulent fluctuations above the buffer layer of wall-bounded flows,” *J. Fluid Mech.* **611**, 215–236 (2008).
- ⁵⁷ P. K. Yeung, “Lagrangian investigations of turbulence,” *Annu. Rev. Fluid Mech.* **34**, 115–142 (2002).
- ⁵⁸ A. E. Perry, S. M. Henbest, and M. S. Chong, “A theoretical and experimental study of wall turbulence,” *J. Fluid Mech.* **165**, 163–199 (1986).
- ⁵⁹ A. A. Townsend, “Equilibrium layers and wall turbulence,” *J. Fluid Mech.* **11**, 97–120 (1961).
- ⁶⁰ H. Lamb, *Hydrodynamics*, 2nd ed. (Cambridge University Press, 1895).
- ⁶¹ G. K. Batchelor, *An Introduction to Fluid Dynamics* (Cambridge University Press, 1967).
- ⁶² This limit is obtained by noting that the motion conserves the energy $\log |\sin(2z_0)|$, and equating the energies of the two configurations in which the rows are either aligned along the centerline, $z_0 = \pi/4$, or maximally separated at $z_0 = iH$.
- ⁶³ J. Jiménez, M. Uhlmann, A. Pinelli, and G. Kawahara, “Turbulent shear flow over active and passive porous surfaces,” *J. Fluid Mech.* **442**, 89–117 (2001).
- ⁶⁴ R. García-Mayoral and J. Jiménez, “Scaling of turbulent structures in riblet channels up to $Re_\tau \approx 550$,” *Phys. Fluids* **24**, 105101 (2012).